recycling

MDPI

Article

Adsorptive Removal of Phosphate from Water Using Aluminum Terephthalate (MIL-53) Metal–Organic Framework and Its Hollow Fiber Module

Shein-Fu Wu and Hsin-Ming Cheng *

Core Facility Center, National Cheng Kung University, Tainan 70101, Taiwan; z9309025@ncku.edu.tw
* Correspondence: smcheng@gs.ncku.edu.tw

Abstract: The aluminum terephthalate (MIL-53) metal–organic framework (MOF) (MIL-53(Al)) was evaluated as an adsorbent for removing phosphates from aqueous solutions. XRD and FTIR were used to confirm the molecular structure. TGA/DSC was used to measure its stability. The green synthesizing MIL-53(Al) showed good performance as a highly efficient adsorbent. The adsorbed MIL-53(Al) nanoparticles still retain their original morphology according to SEM, allowing it to be easily separated from the aqueous solution via filtration. Additionally, the thermal stability of synthesized MIL-53(Al) is capable of withstanding temperatures up to 500 °C, as confirmed by TGA/DSC. Using different initial concentrations of Na_2HPO_4 and ICP-OES measurements, we determined the adsorption values of Na_2HPO_4 by MIL-53(Al) as a function of time. Three kinetic models (pseudo-first-order, pseudo-second-order, and Elovich) and three isotherm models (Langmuir, Freundlich, and Temkin) were used to evaluate the phosphate adsorption behavior of MIL-53(Al) powder in Na_2HPO_4 aqueous solution. Error functions are used to evaluate various kinetic and isotherm models related to different physical processes. From the analysis of the adsorption experiments, the Elovich model is the best-fitting kinetic model, showing that the adsorption rate decreases with increasing adsorption capacity. Furthermore, error function analysis identified the Freundlich model as the most suitable, indicating that complicated adsorption coexists with physisorption, and chemisorption synergistically drives the adsorption process. The module utilizing MIL-53(Al) hollow fibers also demonstrated preliminary attempts at phosphate adsorption and desorption for the first time. This work demonstrated that MIL-53(Al) is an exceptionally stable adsorbent for removing phosphate from contaminated wastewater.

Keywords: metal–organic framework; MIL-53(Al) phosphate; kinetic model; isotherm model; error function; hollow fiber

check for updates

Citation: Wu, S.-F.; Cheng, H.-M. Adsorptive Removal of Phosphate from Water Using Aluminum Terephthalate (MIL-53) Metal–Organic Framework and Its Hollow Fiber Module. *Recycling* **2024**, *9*, 74. https://doi.org/10.3390/recycling9050074

Academic Editor: Giovanni De Feo

Received: 22 July 2024
Revised: 22 August 2024
Accepted: 3 September 2024
Published: 5 September 2024

Copyright: © 2024 by the authors. Licensee MDPI, Basel, Switzerland. This article is an open access article distributed under the terms and conditions of the Creative Commons Attribution (CC BY) license (https://creativecommons.org/licenses/by/4.0/).

1. Introduction

Phosphorus is a naturally limited element found on Earth in numerous compound forms, such as the phosphate ion (PO_4^{3-}), located in water, soil, and sediments [1]. Based on current extraction rates, phosphorus is expected to reach its peak by 2030 and be completely depleted by the end of this century. Unlike alternative energy sources, the phosphorus shortage crisis cannot be mitigated by substituting with another element [2,3]. In the natural cycle, weathering releases phosphorus from rocks into the soil, where it is absorbed by plants, enters the food chain, and circulates among all living organisms [4]. The phosphate ion is an essential component of life which forms the backbone of DNA and cell membranes and is a critical part of adenosine triphosphate (ATP) molecules [5]. Phosphorus is also a widely used industrial chemical [6,7], and, like nitrogen (N) and potassium (K), it is one of the indispensable fertilizer elements in agriculture. However, research shows that only about 15% of the phosphorus applied is absorbed by plants, with the remainder lost to the soil or nearby water bodies. Farmers must therefore reapply fertilizers repeatedly, leading to waste and excessive runoff. While this temporarily increases crop yields, it causes

long-term soil acidification [8,9]. In addition, when agricultural land is overfertilized, phosphates that are not used by plants can be lost from the soil through leaching and water runoff, eventually entering waterways, lakes, and estuaries. Excess phosphates can cause excessive plant growth in waterways, lakes, and estuaries, leading to eutrophication [10]. Accordingly, the environmental and economic losses are incalculable.

The recycling and reuse of phosphorus or phosphate is a very important issue for agriculture and even the social environment. Technically, there are various previous studies that have shown many kinds of approaches to removing phosphates from aqueous solutions, such as sedimentation [11,12], flotation [13], electrocoagulation [14,15], and adsorption [16–24] methods. In this study, the adsorption method was evaluated for phosphate removal as it is a simple process with a lower initial cost than other methods. Activated carbon, dolomite, and hydroxyapatite were chosen as low-cost adsorbents. The results obtained show that both adsorbents have high phosphate adsorption capacity even in a nitrate environment [17,18]. Hydroxyapatite proved to be the most efficient adsorbent; however, it showed a low percentage of desorption, which led to few possibilities of reuse. Dolomite, contrastingly, allows for the desorption of the adsorbed material, which favors its reuse. Moreover, some studies have reported the use of layered double hydroxide (LDH), a layered structure composed of divalent and partially substituted trivalent cations, such as MgAl, MgFe, ZnAl, ZnFe, and CaFe, etc. [19–21]. The interlayer space is composed of anions and water molecules to balance the overall charge. The anion in the middle and the interlayer's interactions are weak and can usually be exchanged to achieve the purpose of adsorbing phosphate. In recent years, many nanostructured and mesoporous crystals have been used as adsorbents, such as nano-alumina, mesoporous silica, TiO_2/Zeolite nanocomposites, etc. [22–24]. Nanocomposites are materials that use their own surface area or the pores within their structure to function as adsorbents. Recently, the adsorption method was evaluated for phosphate removal because it is a simple process with a lower initial cost than other methods. Adsorption methods effectively control the amount of phosphate in wastewater and are considered environmentally friendly.

Metal–organic frameworks (MOFs), reported since the late 20th century, represent a scientifically compelling and functionally evolving new class of mesoscopic, microporous, and ultra-microporous materials [25–33]. MOFs are composed of metal nodes and organic linkers, forming a three-dimensional network structure with ultra-high porosity and surface area. They are flexible and customizable; we can select different metals and organic ligands to achieve specific functions. Because of their high porosity and surface area, MOFs have excellent adsorption capacity and were initially widely used in the storage and separation of gases such as hydrogen, carbon dioxide, and methane [34–37]. In addition, MOFs were utilized for chemical separations and drug delivery systems [38,39]. With their tunable structures and active sites, MOFs show great potential in heterogeneous catalysis as well [40]. In terms of environmental remediation, MOF emerging materials are used in water treatment, and the adsorption and removal of hazardous substances, heavy metals, and organic pollutants are also widely studied [41–52]. For wastewater, most studies prioritize the adsorption and recovery of precious metals or heavy metals and poisons that are immediately toxic to life. In addition to studying the adsorption behavior of MOF materials themselves, there are already studies that use electrostatic spinning and other methods to form fibrous or modified/derived braided networks as efficient adsorbents or filters [48–52]. However, at present, only a few MOFs (NH_2-MIL-101(Al/Fe) and UiO-66-NH_2) have been reported with respect to the adsorption of phosphate in water [53–55]. Furthermore, no concept has yet been proposed for the recycling or reuse of the recovered phosphate which was separated from the MOF adsorbents.

Here, based on the advantages of MOF materials in adsorbing harmful substances in water, we synthesized aluminum terephthalate, MIL-53(Al), using a green process similar to that in a previous report [56]. The basic structure of MIL-53(Al) is a 3D framework with a 1D diamond ring, which is formed via the self-assembly of $AlO_4(OH)_2$ octahedrons with the carboxyl groups of terephthalic acid [57,58]. These properties give MIL-53(Al)

good stability in both neutral and acidic solutions [59]. MIL-53 series MOFs have also attracted attention due to their unique "breathing effect" [60], which causes an abrupt structural change between the large-pore (lp) and narrow-pore (np) forms by introducing different guest molecules, denoted here as MIL-53(Al)$_{lp}$ and MIL-53(Al)$_{np}$, respectively [61]. Interestingly, the change in the breathing state does not depend only on the adsorption stress but can also be stimulated by mechanical pressure, temperature, or even an electric field to enhance adsorption [62]. In this study, we use pseudo-first-order, pseudo-second-order, and Elovich models to explore the adsorption kinetic model of phosphate using MIL-53(Al). We apply the hybrid MIL-53(Al)/polymer hollow fiber module to explore the adsorption and desorption of static and dynamic phosphate solutions for the first time. Due to the unique structures and versatility of MIL-53(Al), we expect that its research will continue to attract widespread attention in materials science due to the potential applications of their controlled release properties.

2. Sample Preparation and Experiments

2.1. Materials and Synthesis MIL-53(Al)

Aluminum nitrate nonahydrate ($Al(NO_3)_3 \cdot 9H_2O$), 1,4-benzenedicarboxylic acid (H_2BDC, >98%), and sodium phosphate dibasic anhydrous, ($Na_2HPO_4 \geq 98\%$) were purchased from Sigma Aldrich. N,N-Dimethylformamide (DMF), methanol, ethanol, and acetone were provided by Merck. All chemicals were used without further purification. Deionized water (DI-water) was collected from a Synergy® UV water purification system (Merck Millipore). The MIL-53(Al) nanocrystalline in this work were synthesized as described in previous literature [56]. Briefly, $Al(NO3)_3 \cdot 9\ H_2O$ (12 mmol; 4.495 g) and H_2BDC (10.8 mmol; 1.8 g) were mixture together then placed in 60 mL of solvent (water and methanol 1:1 v/v) and stirred vigorously at room temperature for 20 min and transferred to an 80 mL Teflon-lined stainless steel autoclave. The reaction mixture was heated to 120 °C for 8 h, after which the product was separated via centrifugation (5000 rpm for 20 min). The detached crystalline material was then washed with DMF three times and acetone once. The as-synthesized powders (light gray in color) were dried at 150 °C for 24 h then allowed to cool naturally. Prior to the experiment, a specific amount of powder will be heated to 300 °C in a vacuum furnace for 10 min as an activation process.

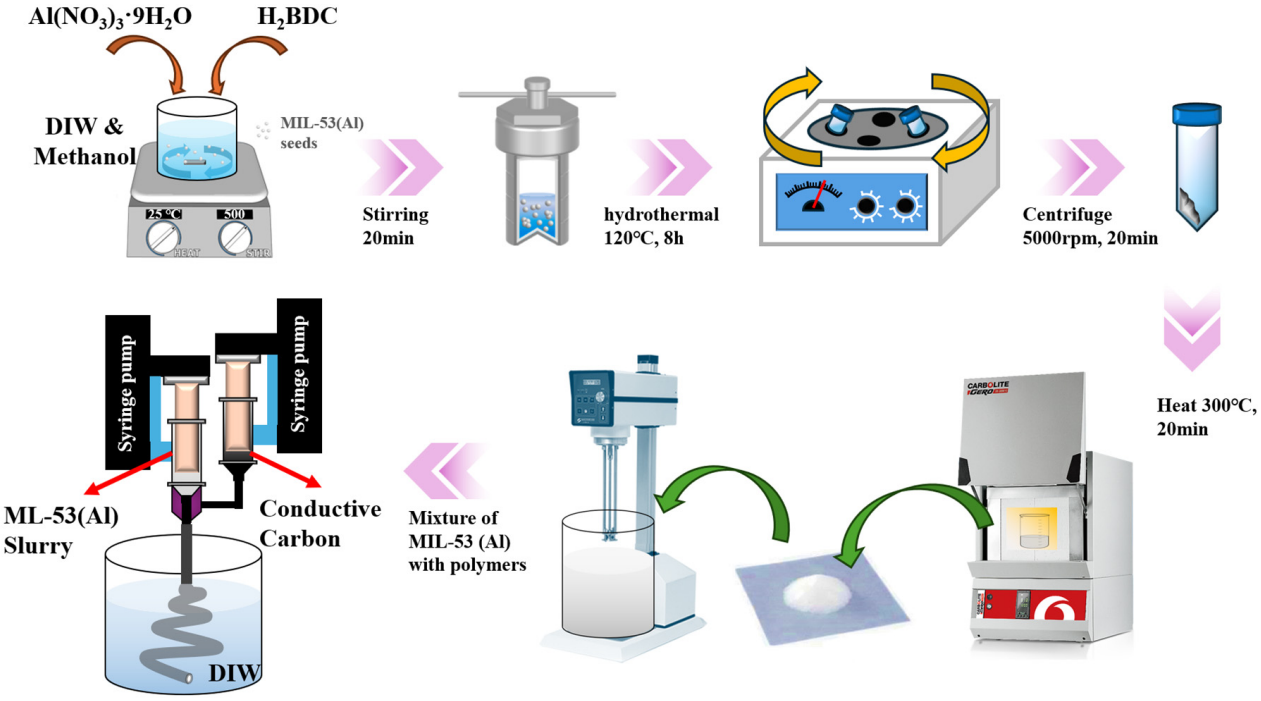
2.2. MIL-53(Al) Hollow Fiber

The MIL-53(Al) hollow fibers were commissioned to be made by AuraMat Co., Ltd., Hsinchu, Taiwan. Those seeking a more-detailed preparation method can refer to the company's patents [63,64]. In this study, we designed hollow fibers with an outer diameter of about two millimeters and an inner diameter of one millimeter. The fiber wall used labor-synthesized MI-53(Al) nano powders with the outer layer covered with highly conductive carbon. The entire demonstration module consists of hundreds of single hollow fibers tightly attached to a single tube bundle with a circumference of 2.5 cm using resin. The length is limited to about 10 cm and then placed in the water filter tube. In this study, the preparation flowchart of hollow fibers and MIL-53(Al) powders is shown in Scheme 1.

2.3. Characterization

The morphology and composition of samples were characterized via scanning electron microscopy (SEM, Hitachi SU-5000, Tokyo, Japan) equipped with an energy-dispersive x-ray spectroscopy (EDS, EDAX Elite, Berwyn, IL, USA), operated at an accelerating voltage of 15 kV. The crystal structure was obtained using an x-ray diffractometer (XRD, Bruker D8 DISCOVER, Karlsruhe, Germany) with Cu Kα radiation (λ = 1.5418 Å). The Rietveld analysis was conducted with FullProf software. The molecular vibrational modes were performed via Fourier transform infrared spectroscopy (FTIR, PerkinElmer Frontier MIR, Waltham, MA, USA) using the transmission technique in a range from 500 to 4000 cm^{-1}. The thermogravimetric analyzer (TGA) and differential scanning calorimeter (DSC) were combined in a TGA/DSC 3+ simultaneous thermal analyzer (Mettler Toledo, New Castle,

DE, USA) with inner gas of argon. The concentration of phosphate in the solution samples before and after the adsorption experiment was confirmed via inductively coupled plasma optical emission spectrometry (ICP-OES, iCAP 6000 series Thermo-Scientific, Waltham, MA USA).



Scheme 1. Production flow chart of the MIL-53(Al) powders and corresponding hollow fibers.

3. Results and Discussion

3.1. Characterization of Synthesized MIL-53(Al)

As shown in Figure 1a, owing to the copious breathing of the mesoporous MIL-53(Al) nanocrystalline, after we use the low-temperature activation procedure, the crystalline phase of the powder still appears to be in the MIL-53(Al)$_{lp}$ and MIL-53(Al)$_{np}$ coexisting crystal phases. We can see the main XRD diffraction peaks of the MIL-53(Al)$_{lp}$ phase (peak #1 at 8.75°) and the MIL-53(Al)$_{np}$ phase (peak #2 at 9.37°), respectively. The synthesized crystal structure in this study is similar to that in previous studies [65,66]. Since the experiment will be carried out in water, there is no need to obtain pure MIL-53(Al)$_{lp}$, which would typically require higher temperatures for sample activation procedures [58]. When the powder was immersed in deionized water for two hours, we observed that the MIL-53(Al)$_{lp}$ signal in the XRD diffraction pattern of the dried powder was greatly attenuated. This attenuation is related to the aforementioned breathing effect, especially when the powder undergoes hydration [58]. Interestingly, when using disodium hydrogen phosphate (Na_2HPO_4) as a contamination source within an aqueous solution, we immersed 330 mg MIL-53(Al) into an 80 ppm Na_2HPO_4 aqua liquid for 2 h and 4 days and then dried it for XRD analysis. There were significant changes in the lattice structure. It gradually changed from orthorhombic ($a \neq b \neq c$ and $\alpha = \beta = \gamma$) (pristine and in DIW) to monoclinic ($a = b = c$ and $\alpha = \gamma$, $\beta > 90°$) (2 h in Na_2HPO_4 solution) and then swelled and disintegrated (4 days in Na_2HPO_4 solution). The crystallite or grain size d of the samples was determined using the Scherrer equation $d = 0.9\lambda/B\cos\theta$, where λ is the X-ray wavelength, B is the full-width-at-half-maximum of the selected peak, and θ is the peak position [67]. These results are shown in the Supporting Information (Table S1). Ten major peaks were used to calculate the average d (as shown in Figure 1a). The smallest d of 29.30 Å was observed for pure MIL-53(Al). A gradual increase in the crystallite size was observed when MIL-53(Al) was immersed in DI-water or Na_2HPO_4 for 2 h or 4 days, with values of 30.00 Å, 39.23 Å,

and 39.64 Å, respectively. The detailed lattice structures of MIL-53(Al)$_{np}$ in each state and their corresponding volumes are listed in Table 1. The structure of MIL-53(Al) is affected by adsorbed guests. The kinetic diameter of the water molecules is about 2.6 Å, which is smaller than the pore size of MIL53 (~3.6 Å) [60]. However, the size of the phosphate is about 3 Å, which is close to the MIL-53(Al) pore size. The adsorption capacity is bound to have a saturation limit. When the crystal absorbs too many phosphate groups, it will easily cause structural distortion. In addition, it has been reported that MIL-53(Al) has a better effect on adsorbing organic matter in a weakly acidic environment, but its structure is easily destroyed in a strong alkaline solution [68]. The above reasons also explain the reason why the MIL-53(Al) structure would be damaged due to excessive immersion time in the phosphate solution. We also observed the small signal of the AlPO4 compound in the XRD pattern, which appeared after prolonged immersion in Na_2HPO_4 solution, as shown in Figure S1.

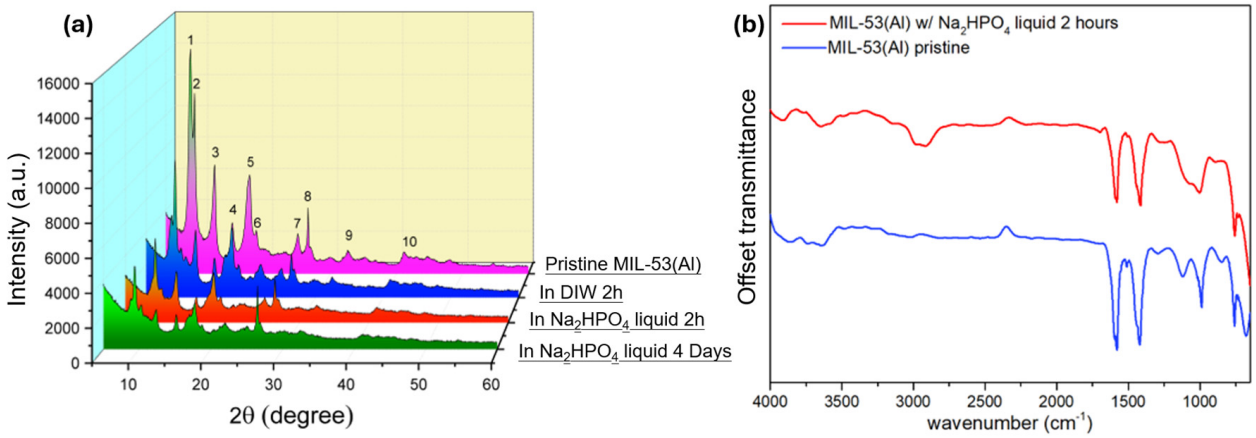


Figure 1. (**a**) XRD patterns (from top to bottom) of pristine MIL-53(Al) powders, MIL-53(Al) powders immersed in DIW for 2 h then dried, MIL-53(Al) immersed in phosphate liquid for 2 h then dried, and MIL-53(Al) powders immersed in phosphate liquid for 4 days then dried. (**b**) FTIR spectra of the dried MIL-53(Al) powders before and after adsorption of phosphate for 2 h.

Table 1. Unit cell parameters for the experimental MIL-53(Al) samples.

Samples	Space Group	Unit Cell Parameters			Volume (Å^3) of Unit Cells
MIL-53(Al)$_{lp}$	*Imcm* (no. 74)	a = 16.9050 Å α = 90.000°	b = 6.6664 Å β = 90.000°	c = 12.7503 Å γ = 90.000°	1436.9036
MIL-53(Al)l$_p$ in DIW 2 h	*Pnma* (no. 62)	a = 16.2430 Å α = 90.000°	b = 6.6352 Å β = 90.000°	c = 13.4943 Å γ = 90.000°	1454.3556
MIL-53(Al)$_{np}$ in Na_2HPO_4 (aq) 2 h	*C2/c* (no. 15)	a = 5.1620 Å α = 90.000°	b = 8.7892 Å β = 93.536°	c = 20.8115 Å γ = 90.000°	942.4028
MIL-53(Al) in Na_2HPO_4 (aq) 4 days	N/A	a = 13.7614 Å α = 90.000°	b = 13.7614 Å β = 90.000°	c = 14.7840 Å γ = 120.000°	2424.6431

The FTIR spectrum of the pristine MIL-53(Al) is shown in Figure 1b. The strong adsorption peaks at 1577 cm^{-1} and 1508 cm^{-1} are attributed to the dissymmetry of the stretching of the CO_2 ($\nu_{as}CO(CO_2)$ of O–C–O). The adsorption peaks at 1508 cm^{-1} and 1420 cm^{-1} are attributed to the symmetric stretching vibration $\nu_{as}CO(CO_2)$ of O–C–O and O–C=O stretch of MIL-53(Al). These values are consistent with the presence of CO_2 groups coordinated with Al atoms. In addition, the adsorption peak at 1699 cm^{-1} was attributed to the encapsulated molecules of free terephthalic acid within the pores of the MIL-53(Al) structure in their protonated form –CO_2H [58]. The band at 1400–1700 cm^{-1} contains the characteristic adsorption peaks of the carboxyl functional groups in MIL-

53(Al) [69]. The narrow adsorption band at 3642 cm^{-1} was due to the stretching mode of O–H [70]. The broad peaks at around 1000 and 1200 cm^{-1} and the peak at 677 cm^{-1} were attributed to the in-plane bending, δ(C-H), and out-of-plane bending, γ(C-C-C), of the benzene ring, respectively [71]. In addition, the band at 670–1000 cm^{-1} is related to the stretching vibration of C–H from the benzene ring [72]. A preliminary comparison of the spectra of the two samples shows that there are only slight differences. In addition to the in-plane deformation of the aromatic ring, the signal changes to the weaker in-plane bending peaks of the aromatic ring, and then there are the band peaks observed around 3600–3900 cm^{-1}, which are attributed to the bending and stretching –O-H modes of water. After the adsorption experiments, a relatively intense broad band is centered at around 3000 cm^{-1} and is attributed to the –O–H stretch from water. This is reasonable, since this sample has been soaked in water.

The thermal stability of the MIL-53(Al) adsorbent is a crucial factor that determines its operational temperature window. The thermal stability of as-received MIL-53(Al) was analyzed via TGA/DSC from 35 to 750 °C in an inert Ar atmosphere, as shown in Figure 2. The red line showing the TGA curve of the MIL-53(Al) powder shows two weight-loss steps. The weight started decreasing at approximately 100 °C, which corresponds to the evaporation of adsorbed water molecules from the adsorbent particles. Subsequently, the second weight-loss period started at ~500 °C due to the collapse of the MIL-53(Al) framework [72,73]. A previous study attributed the weight loss to the decomposition of organic ligands in terephthalic acid, where the final residue was Al_2O_3 [72]. This can explain the thermal stability of MIL-53(Al) up to 500 °C. Hence, the operational temperature for MIL-53(Al) should not exceed 500 °C. The simultaneous DSC results (blue line) showed that an endothermic state began around 100 °C. Above 500 °C, the rate of the endothermic reaction rapidly increased and was then suddenly replaced by an exothermic reaction at 550 °C due to the combustion reaction, which then showed a solid–liquid transition (e.g., melting) at around 600 °C [57]. This is consistent with the two-stage weight-loss process during heating and the removal of surface-adsorbed and encapsulated terephthalic acid within the large-breathing framework [58].

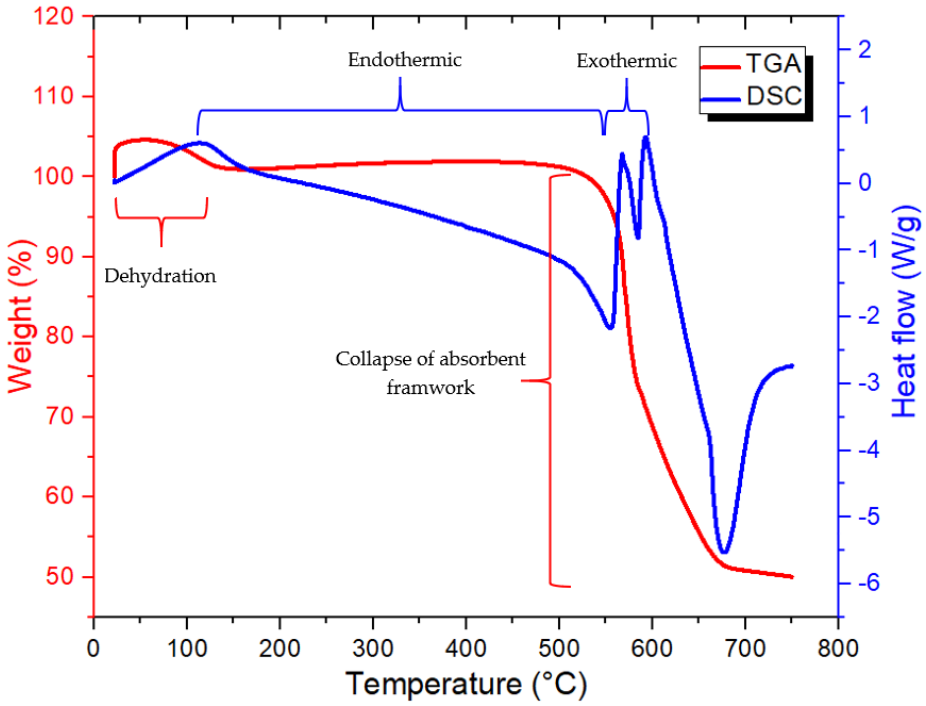


Figure 2. TGA and DSC curves of the pristine MIL-53(Al) over the temperature range of 35–750 °C heated at 10 °C per min.

The results of the SEM/EDS analysis for the pristine MIL-53(Al), as well as the adsorbent after 2 h and 4 days of Na_2HPO_4 adsorption, are shown in Figure 3. Figure 3a,f,k show the color graphic overlay of different elements of dry MIL-53(Al) powders in pristine condition, after 2 h Na_2HPO_4 adsorption, and after 4 days Na_2HPO_4 adsorption. Before adsorption (Figure 3a–e), only O (Figure 3b) and Al (Figure 3c) were detected in significant quantities as the composition of MIL-53(Al) is $C_8H_5AlO_5$, in which the light elements, such as C and H, cannot be quantified by EDS. The morphology of MIL-53(Al) is shown in Figure S2a. No chemical reaction occurred with moisture from the air under ambient conditions at approximately 25 °C and humidity under 50%. Based on the XRD results, the change in environmental temperature was not expected to affect the internal structure significantly, causing it to transition between the narrow-pore and large-pore states [72]. After 2 h of Na_2HPO_4 adsorption (Figure 3f–j), the MOF particles appeared slightly clustered, with larger particles observed (Figure 3f). The Na_2HPO_4 was indeed adsorbed by the MIL-53(Al), as indicated by the presence of P (Figure 3i) and Na (Figure 3j) elements in the mapping images, alongside O (Figure 3g) and Al (Figure 3h). After 4 days of Na_2HPO_4 adsorption (Figure 3k–o), the MOF particles appeared relatively dispersed. It is obvious that the shape is not uniform, and the crystallization is poor. The situation in which the pristine MIL-53(Al) crystalline particles and comparative morphologies became aggregated and then dispersed, adsorbing Na_2HPO_4 for 2 h and 4 days, respectively, can be observed in more detail in the SEM images (Figure S2). This is consistent with the phenomenon observed via XRD.

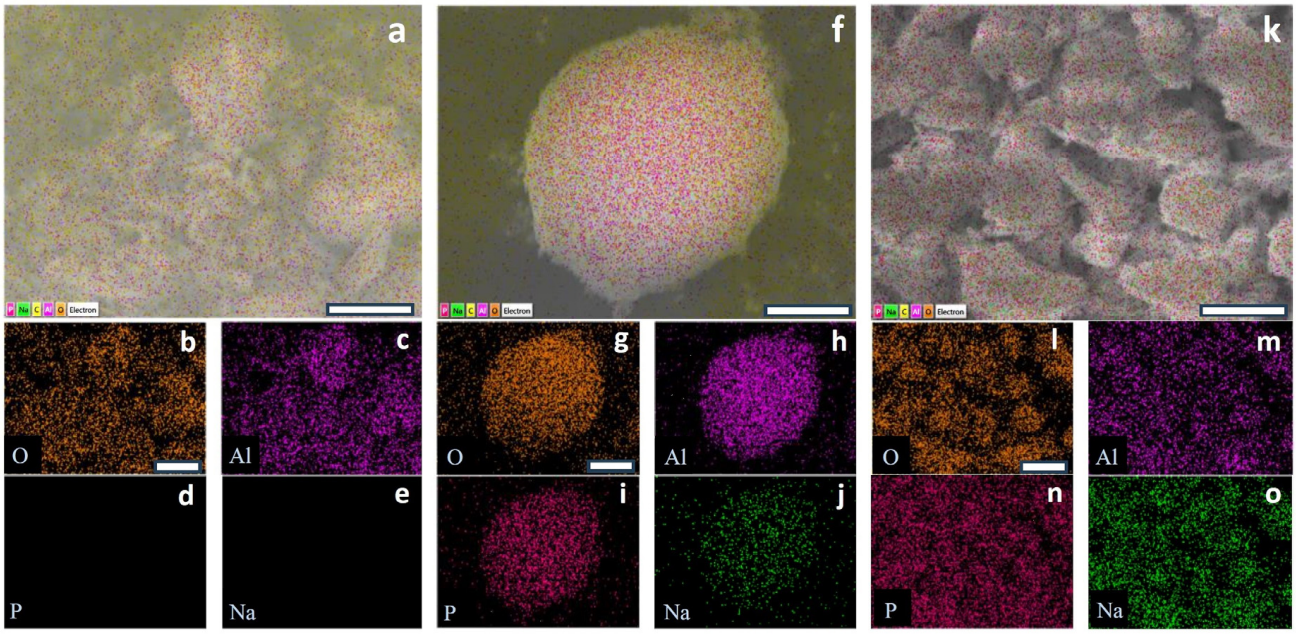


Figure 3. EDS analysis of the MOF samples before and after adsorption: (**a**) mixed elements, (**b**) Al, (**c**) O, (**d**) P, and (**e**) Na maps of the pristine MIL-53(Al) powders; (**f**) mixed elements, (**g**) Al, (**h**) O, (**i**) P, and (**j**) Na maps of the MIL-53(Al) powders after 2 h of Na_2HPO_4 adsorption; (**k**) mixed elements, (**l**) Al, (**m**) O, (**n**) P, and (**o**) Na maps of the MIL-53(Al) powders after 4 days of Na_2HPO_4 adsorption. Scale bar: 2.5 μm.

The EDS quantitative analysis of several major elements (O, Al, P, and Na) is shown in Figure 4. Before adsorption, peaks from only Al (28.1 atomic %) and O (71.9 atomic %) were detected, with contents corresponding to the composition of pure MIL-53(Al). After 2 h of Na_2HPO_4 adsorption, the Al and O peaks were like those of the initial case. In addition, Na and P had concentrations of 3.8 atomic % and 8.4 atomic %, respectively. After 4 days of adsorption, the Na and P contents inside the MIL-53(Al) increased to 11.4% and 19.7%,

respectively. These results indicate that the MIL-53(Al) can distinctly adsorb the Na_2HPO_4 from the aqueous solution.

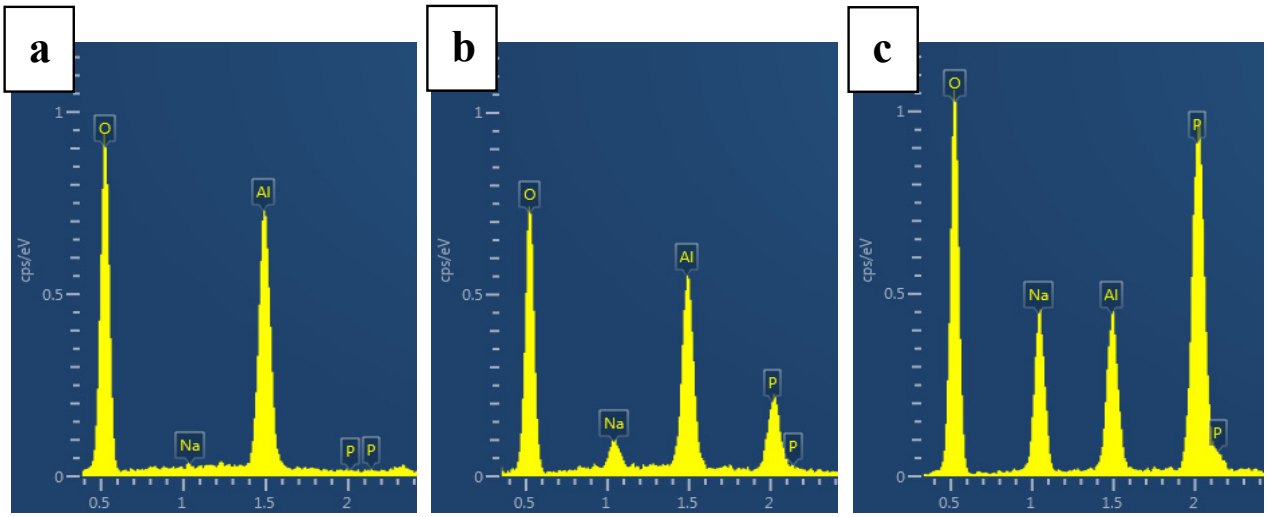


Figure 4. EDS spectra of the MIL-53(Al) (**a**) before and (**b**) after 2 h of Na_2HPO_4 adsorption and (**c**) after 4 days of Na_2HPO_4 adsorption.

3.2. Evolution of Adsorption Kinetic Models

To confirm the ability of MIL-53(Al) to adsorb phosphate, each phosphate solution, with concentrations of about 20, 40, 90, and 250 ppm in 150 mL of DIW, was mixed with MIL-53(Al) powders at a ratio of 330 mg·L^{-1}; that is, various amounts of phosphate powders (22.7, 44.6, 89.6, and 245.1 mg) were dissolved in 100 mL of DIW and mixed with 33 mg of MIL-53(Al). The entire mixed solution system was subjected to strong stirring to prevent precipitation. After adsorption for a predetermined time, a small amount of solution was extracted from the system. The liquid with the MIL-53(Al) adsorbents inside was filtrated using a 0.45 µm syringe filter (hydrophobic PTFE). ICP-OES was used to determine the phosphorus concentration of the supernatant.

As shown in Figure 5, at a phosphate concentration of 22.7 ppm, after 4 days of adsorption, almost all the phosphate was removed from the aqueous solution, with only 0.05 ppm remaining. Additionally, at concentrations of 44.6, 89.6, and 245.1 ppm, the MOF continued to adsorb the phosphate over 4 days. These results confirm that the MIL-53(Al) can adsorb more than its own weight in phosphate. Notably, by calculation, for a phosphate concentration of 245.1 ppm, the MIL-53(Al) can adsorb 77 mg PO_4^- after 4 days (with 168 ppm remaining, as detected via ICP-OES). Hence, after 4 days, the amount of adsorbent was already double that of the adsorbate, and the equilibrium stage had not been reached. This was attributed to the breathing behavior of MIL-53(Al), which allows it to continuously adsorb the adsorbate due to its flexible pore structure, even after long time of adsorption. The ICP-OES results were fit using various kinetic and isotherm models, as described in the following section.

The amount of phosphate adsorbed per unit mass of adsorbent at time t (Q_t, mg g^{-1}) and at equilibrium (Q_e, mg g^{-1}) could be calculated using Equations (1) and (2) [68,74]:

$$Q_t = \frac{C_0 - C_t}{m} \cdot V, \quad (1)$$

$$Q_e = \frac{C_0 - C_e}{m} \cdot V. \quad (2)$$

Here, C_0 is the initial concentration of adsorbate in the solution (mg·L^{-1}), m (g) is the mass of adsorbent in the solution (g), and V (L) is the volume of solution.

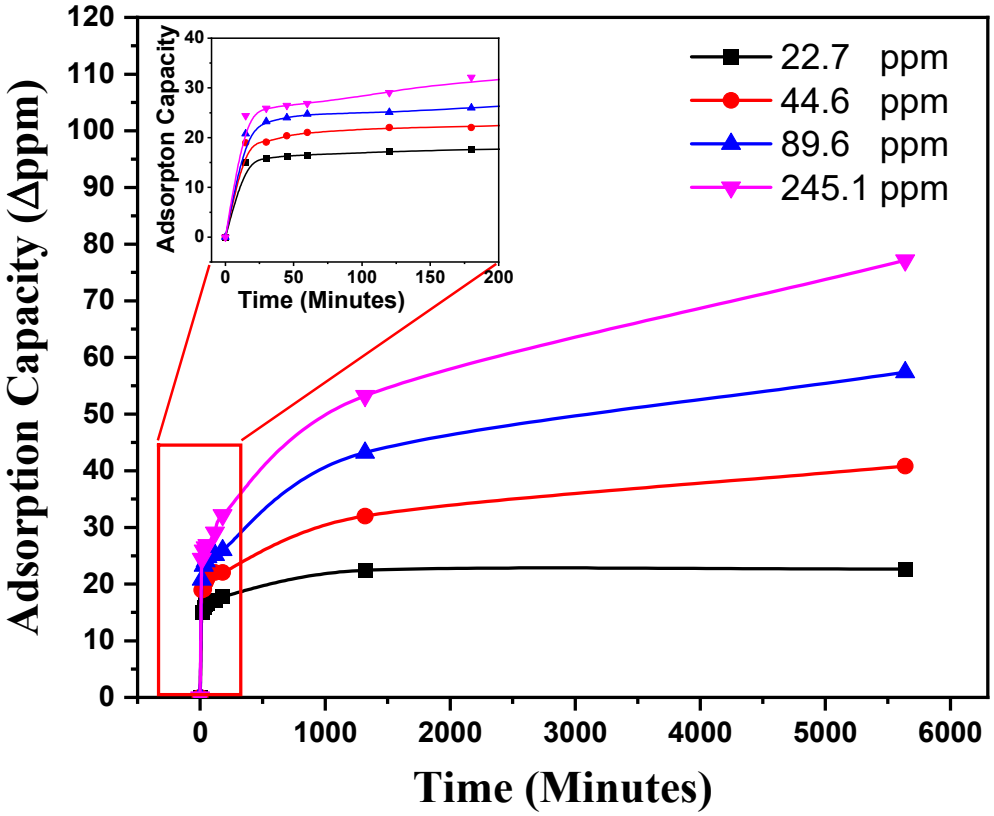


Figure 5. Concentration reduction of different phosphate aqueous solutions before and after MIL-53(Al) adsorption. Concentration was confirmed using ICP-OES with phosphorus.

There are two main processes that can occur during adsorption: physical (physisorption) and chemical (chemisorption), which are differentiated by the nature of the attractive forces [75]. Physisorption is caused by intermolecular forces (e.g., van der Waals forces) between the adsorbates and the adsorbent. In contrast, chemisorption involves the formation of chemical bonds between the adsorbate and the adsorbent, including electron-transfer reactions. The adsorption trends of Na_2HPO_4 by MIL-53(Al) were investigated using the batch adsorption experiments described above. The adsorbate molecules attach to the surface of the adsorbent, and the adsorption process in an aqueous solution can be complex. Initially, the adsorption rate was high but then decreased over time. The halt in the adsorption process after approximately one day for the phosphate concentration of 22.7 ppm was attributed to the end of monolayer adsorption. The data also showed that the initial Na_2HPO_4 concentrations influenced the contact time necessary to reach equilibrium and that the sorption capacity increased for the higher initial Na_2HPO_4 concentrations. On the other hand, we found that the adsorption rate is more efficient at low concentrations. At a Na_2HPO_4 concentration of 22.7 ppm, more than 70% of the phosphate was adsorbed by MIL-53(Al) after 1 h, and 98.67% of the Na_2HPO_4 will be adsorbed by MIL-53(Al) in less than 24 h.

Three adsorption kinetic models were used in this study to fit the experimental adsorption data, namely, the pseudo-first-order model (Equation (4)) [76,77], pseudo-second-order model (Equation (5)) [76], and the Elovich model (Equation (6)) [78,79].

$$\ln(Q_e - Q_t) = \ln(Q_e) - k_1 t \quad (3)$$

$$\frac{t}{Q_t} = \frac{1}{k_2 Q_e^2} + \left(\frac{1}{Q_e}\right) t \quad (4)$$

$$Q_t = \frac{1}{\beta} \ln t + \frac{1}{\beta} \ln \alpha\beta \quad (5)$$

Here, k_1 (min^{-1}) and k_2 ($g \cdot min^{-1} \cdot mg^{-1}$) are the pseudo-first-order and pseudo second-order adsorption rates, respectively. Q_e is the amount of phosphate absorbed per mass of adsorbent under equilibrium conditions, and Q_t is the amount of adsorbate adsorbed at time t (min). The constant k_2 is calculated using k_2 = slope^2/intercept when t/Q_t is plotted against t [80]. For the Elovich model, α is the initial adsorption rate ($mg \cdot g^{-1} \cdot min^{-1}$) and β is the desorption constant ($g \cdot mg^{-1}$), where $\alpha, \beta, t \gg 1$ is assumed. Thus, the plot of Q_t vs. In t could provide a linear relationship with the slope of $(1/\beta)$ and intercept of $(1/\beta)$ In $(\alpha\beta)$. For pseudo-first-order model, Figure 6 demonstrates that the adsorption rate is affected by the phosphate concentration, which assumes that the rate of adsorption of the adsorbent decreases the concentration or the adsorbent's performance [68]. The adsorption rate of the pseudo-second-order model is affected simultaneously by both the phosphate concentration and the adsorption performance of MIL-53(Al). For the Elovich model, Q_t exponentially increases as the amount of adsorbed solute increases. However, both the adsorbent concentration and performance are crucial factors in the adsorption process. The nonlinear curve fitting of experimental data can be used to determine the fitting constants and derive the kinetic parameters. The fitting results of the linear regression using the three different models for various phosphate concentrations are listed Table 2. The fitting coefficient (R^2) resulting from the pseudo-first-order model varied depending on the concentration, and the R^2 value for the pseudo-second-order and Elovich models were quite high for all concentrations, while the pseudo-second-order model showed the best fit (with the highest R^2 values). Although the pseudo-first-order and pseudo-second-order models arose from different algorithms, their corresponding Q_e values were similar. Upon approximation by fitting, the R^2 values of the pseudo-second-order model were greater than those of the other models, with values exceeding 0.99 for all adsorbate concentrations. It is assumed that the process may follow pseudo-second-order kinetics and that the rate-limiting step could indicate that the adsorption process is governed by chemisorption, involving valency forces through the sharing or exchange of electrons between the sorbent and sorbate as covalent bonds [74,81–83]. Moreover, the theoretical Q_e calculated from the pseudo-second-order model was in good agreement with the experimental value at the corresponding concentration. Hence, the pseudo-second-order model was the most suitable model for describing the adsorption kinetics of phosphate on MIL-53(Al). Compared with activated carbon, MIL-53(Al) shows a more efficient adsorptive rate and a higher adsorption capacity [84].

3.3. Evolution of Adsorption Isotherm Models

Adsorption experiments were conducted to evaluate the phosphate isotherm on MIL-53(Al). Three isotherm models, Langmuir, Freundlich, and Temkin, were used in this study.

Table 2. Kinetic constants and fitting coefficients of the three different models applied to the experimental data for various phosphate concentrations.

Na_2HPO_4	Pseudo-First-Order Model			Pseudo-Second-Order Model			Elovich Model		
C_0 (mg/L)	k_1 (1/min)	Q_e (mg/g)	R^2	k_2 (g/min·mg)	Q_e (mg g^{-1})	R^2	α	β	R^2
22.7	0.0027	68.6364	0.9091	6.1×10^{-4}	68.97	0.9999	9304.104	0.2322	0.9552
44.6	0.0008	123.6364	0.6972	7.7×10^{-4}	125.11	0.9963	55.631	0.0883	0.9289
89.6	0.0008	173.9394	0.7984	4.1×10^{-4}	175.44	0.9947	18.649	0.0538	0.9166
245.1	0.0018	233.7879	0.9612	2.4×10^{-5}	243.91	0.9925	5.366	0.0297	0.9137

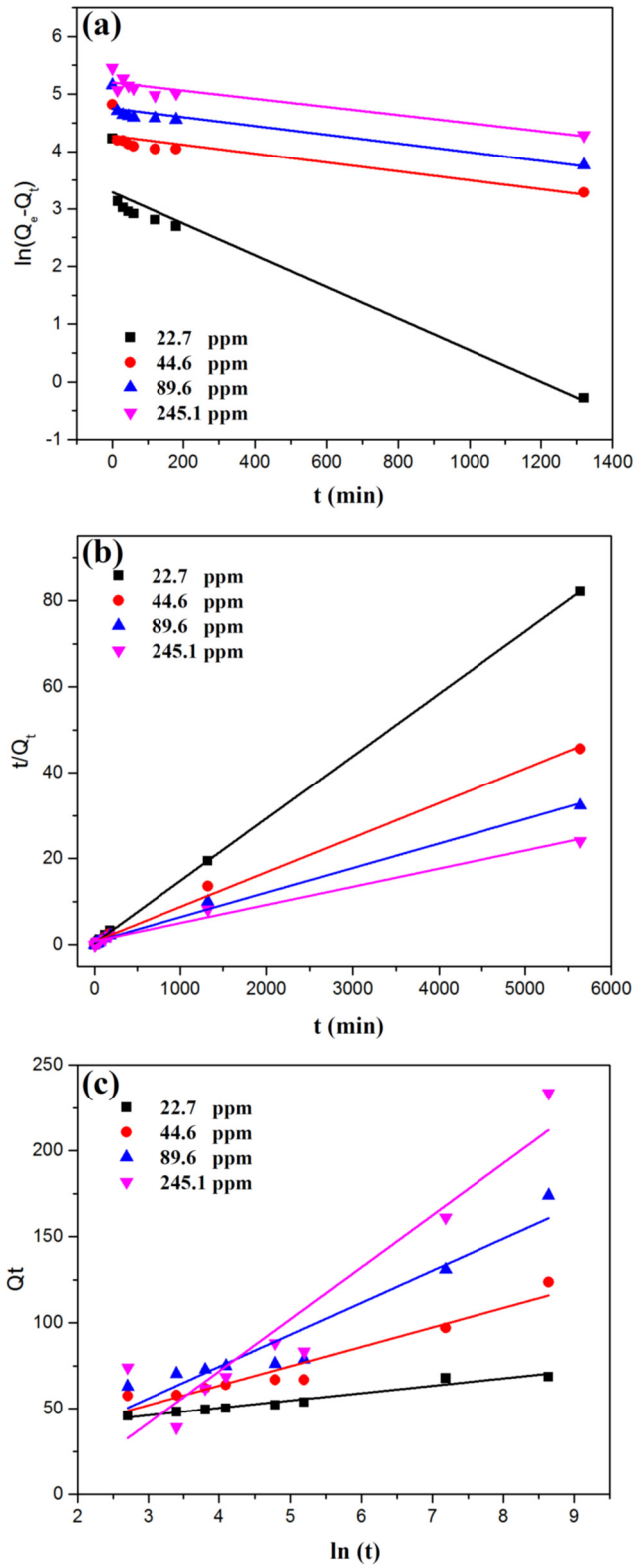


Figure 6. Comparison of various adsorption kinetic models used to fit the experimental data: (**a**) pseudo-first-order model; (**b**) pseudo-second-order model; (**c**) Elovich model.

The Langmuir adsorption isotherm model, represented by Equation (7), describes monolayer adsorption with a constant adsorption energy on a homogeneous adsorption surface where the number of adsorption sites is finite. Once the adsorbate occupies the adsorption sites, no further adsorption can occur. It is assumed that the reaction does not

propagate adsorption in the plane of the surface, and the adsorption remains consistent without interference [85,86].

$$\frac{C_e}{Q_e} = \frac{1}{Q_m k_L} + \left(\frac{1}{Q_m}\right) C_e. \tag{6}$$

Here, C_e is the concentration of the adsorbate in the solution at equilibrium (mg·L^{-1}); k_L is the Langmuir isotherm constant (L·mg^{-1}), where higher values indicate a more favorable adsorption process; [70] and Q_m is the maximum amount of adsorbed adsorbate allowed by monolayer adsorption (mg·g^{-1}). The calculated C_e/Q_e v.s. C_e data are shown in Figure 7a, where the line shows the fitting result, which gave Q_m equal 238.09 from the calculation of the plotting slope, and the Langmuir constant k_L was 0.211. It can be found that the R^2 value of the Langmuir isotherm model was above 0.996.

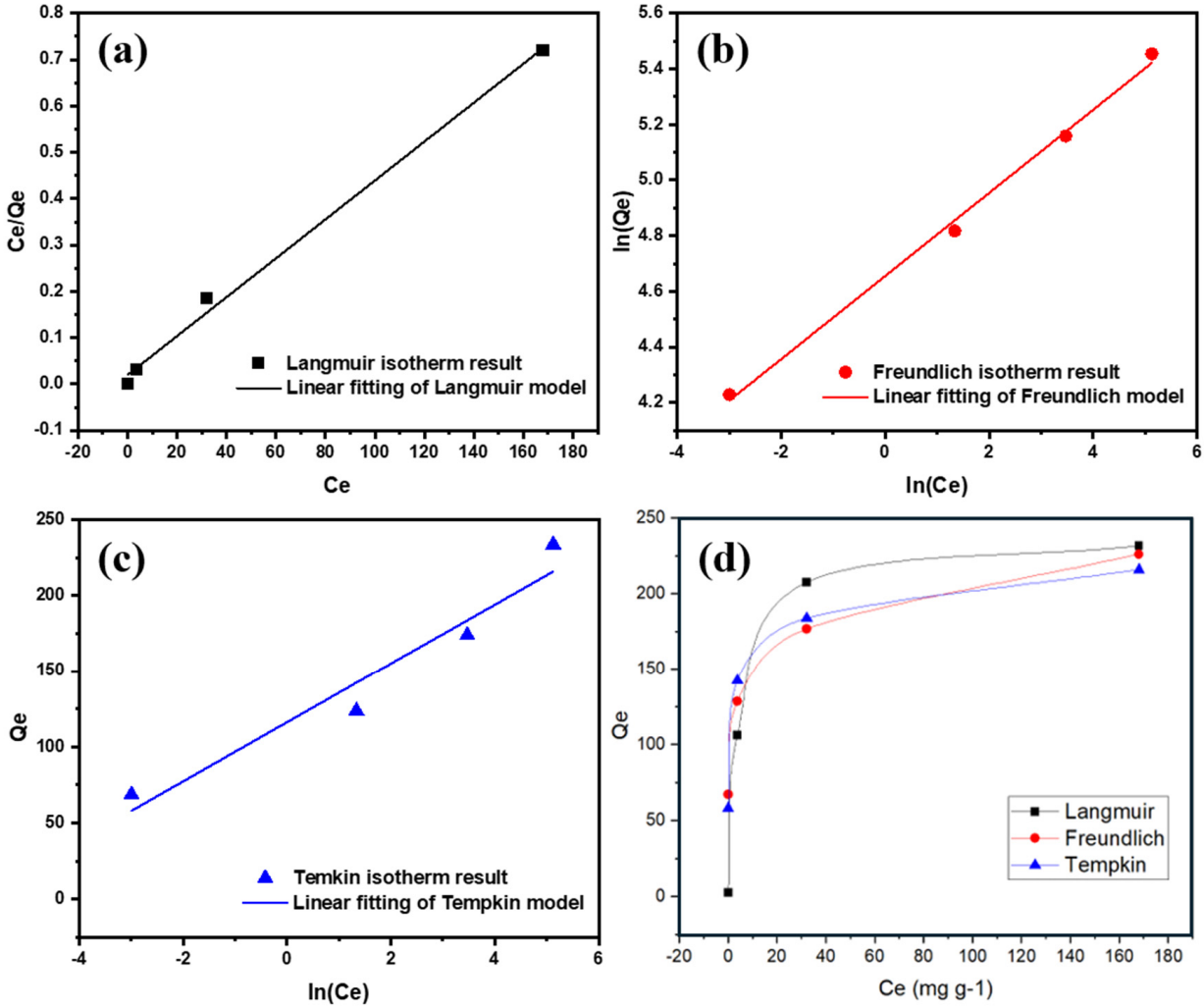


Figure 7. Comparison of various adsorption isotherm models used to fit the experimental data—(**a**) Langmuir isotherm; (**b**) Freundlich isotherm; (**c**) Temkin isotherm—and (**d**) comparison of nonlinear curves of the three isotherm models.

The Freundlich isotherm model was the second principle employed, as shown with the Equation (8) [85]:

$$\ln Q_e = \ln k_F + \frac{1}{n} \ln C_e, \tag{7}$$

where k_f and n are Freundlich constants, corresponding to adsorption capacity and adsorption intensity, respectively. The Freundlich isotherm model assumes that the adsorption

system has monolayer and/or multilayer adsorption, where both chemisorption and physisorption mechanisms are considered [70]. This model is suitable for non-ideal adsorption on heterogeneous surfaces, as well as multilayer adsorption [87–89]. The Freundlich isotherm is a prototype adsorption model that has been widely used in environmental chemistry, and its equation aligns well with the Langmuir equation over moderate concentration ranges. However, unlike the Langmuir model, it does not simplify to a linear isotherm (Henry's law) at low surface coverage. Both models have the limitation that equilibrium data over a wide concentration range cannot be accurately fitted with a single set of constants [87]. For the Freundlich expression, the absorbent molecule with the highest energy will be adsorbed first, until the adsorption energy decreases exponentially as the adsorption process proceeds [90]. For Equation (8), k_F is the adsorption coefficient and represents the adhesion ability of Na_2HPO_4 into MIL-53(Al). This constant can be relative to the adsorption capacity of the absorbent in this study; $1/n$ demonstrates the adsorption property of thee adsorbate onto MIL-53(Al) or surface heterogeneity. The desirable adsorption isotherm can be observed from value of the slope ($1/n$). If the slope is closer to zero, this means that the adsorption behavior becomes more nonlinear and absorbent surface becomes more heterogeneous; whereas a slope below unity indicates that the chemisorption process has occurred; and a slope above 1 indicates a combinative adsorption with both physisorption and chemisorption [91]. Using the linear fitting with an R^2 value of about 0.996, in Figure 7b, we obtained a Freundlich constants with an n-value of 6.69 and a k_F of 105.18, which represents the affinity of the binding sites with the adsorption energy. These data confirm that the experiment is a physical process, and the phosphates in MIL-53(Al) present a normally heterogeneous adsorption. In addition, the scenario where $n > 1$ is the most common and may result from the distribution of surface sites or factors that decrease adsorbent–adsorbate interactions as surface density increases [92]. In any case, values of n within the range of 1~10 indicate a good adsorption system [93,94].

The Temkin isotherm model, which contains a definite factor that explicitly considers the interaction between absorbate and absorbent, was also evaluated. It ignores the extremely low and high value of the concentration and assumes that the heat of the adsorption of all molecules in the layer (the temperature function) would decrease linearly, rather than logarithmically, with coverage due to adsorbent–adsorbate interaction [95]. A similar distribution of characteristics indicates that adsorption quickens the energy up to the maximum binding energy [96]. The Temkin isotherm may be written as

$$Q_e = B_T \ln(A_T) + B_T \ln(C_e). \quad (8)$$

Here, B_T (mg/g) is a constant related to the heat of adsorption determined from the slope of the plot of Q_e vs. C_e, while A_T is the equilibrium binding constant corresponding to the maximum binding energy. ($L \cdot g^{-1}$). From Figure 7c and Equation (9), we determined that B_T = 19.45 and A_T is about 394, with R^2~0.94 for the phosphate solutions. The nonlinear forms of the Langmuir, Freundlich, and Temkin isotherm models also could be expressed as the powerful equations for evaluating Q_e emerged, as shown in Equations (10), (11), and (12), respectively.

$$Q_e = \frac{Q_m k_L C_e}{1 + k_L C_e} \quad (9)$$

$$Q_e = k_F {C_e}^{1/n} \quad (10)$$

$$Q_e = \frac{RT}{b} \ln(A_T C_e) \quad (11)$$

For the Temkin isotherm parameters, the constant $B_T = RT/b$ (in Equation (9)), where R is the universal gas constant (8.314 $J \cdot mol^{-1} \cdot K^{-1}$), T(K) is the absolute temperature, and the parameter $1/b$ is the adsorption potential of MIL-53(Al). The plots of Q_e vs. C_e for all nonlinear adsorption isotherms are also shown in Figure 7d. All fitting results are listed in Table S2. The experimental results show that as the phosphate concentration increased, the adsorption capacity of the adsorbent also increased. Therefore, the concentration of

the solution is a crucial factor influencing the adsorption of Na_2HPO_4 by MIL-53(Al). The small differences between the calculated and experimental results indicate that the error percentages at all concentration levels are acceptable for the numerical analysis of the kinetic models and the isotherm ones. However, the R^2 values determined using the Langmuir, Freundlich, and Temkin isotherm models were 0.99, 0.99, and 0.94, respectively. These numbers are very similar. Accordingly, it is still a major challenge to define and predict the adsorption model more accurately and obtain the adsorption efficiency.

3.4. Evolution by Corresponding Error Functions

Therefore, we precisely calculate the further error functions of the used models. First, the sum of the squares of errors (ERRSQ) is one of the most common error functions; the liquid phase concentration level is especially high [97]. Hence, the ERRSQ quality will increase as the adsorbate concentration increases. Second, the average relative error (ARE), which evaluates the tendency of the model to under- or overestimate the experiment values, can be used to decrease the fractional error over the entire concentration range [98]. Finally, the hybrid fractional error function (HYBRID) was developed to improve the ERRSQ analysis at low concentrations [99]. Furthermore, it uses the degrees of freedom of the system minus the number of parameters of the isotherm as a divisor [98,100]. The three error functions were used to analyze the applicability of the kinetic and isotherm models. The ERRSQ, ARE, and HYBRID error functions are shown in Equations (12)–(14), respectively.

$$\sum_{i=1}^{n}(Q_{e,i,calc} - Q_{e,i,meas})^2 \tag{12}$$

$$\frac{100}{n}\sum_{i=1}^{n}\left|\frac{Q_{e,i,calc} - Q_{e,i,meas}}{Q_{e,i,meas}}\right| \tag{13}$$

$$\frac{100}{n-p}\sum_{i=1}^{n}\frac{(Q_{e,i,calc} - Q_{e,i,meas})^2}{Q_{e,i,meas}} \tag{14}$$

The results of the error function for the kinetic models are shown in Table 3. All three error functions gave very high error values for the pseudo-first-order and pseudo-second-order models and much smaller values for the Elovich model. Although the pseudo-second-order model showed the highest R^2 value, the overall results showed that the Elovich model is the best kinetic model for describing our system.

Table 3. Results of the error function analysis of the kinetic models at room temperature (RT).

Kinetic	C_0 (ppm)	ERRSQ	ARE	HYBRID
Pseudo-first-order	22.7	1823.01	5.25	22.77
	44.6	2971.53	7.57	54.54
	89.6	3834.21	7.88	73.32
	245.1	5894.43	16.52	463.37
Pseudo-second-order	22.7	581.69	12.34	205.52
	44.6	4046.08	28.81	1102.48
	89.6	6251.15	31.82	1427.87
	245.1	8079.57	22.77	1205.00
Elovich	22.7	24.44	2.30	6.53
	44.6	276.10	6.44	64.64
	89.6	885.69	10.49	177.35
	245.1	3905.51	20.22	689.24

The error functions were further used to evaluate the isotherm models as well, as shown in Table 4, where the error results indicate the deviation between the experimental data and fitting values. Although the Langmuir isotherm gave the highest error values (above 0.996) for all error functions compared to the other isotherm models, its ERRSQ

value was much higher than the other isotherm models. The Freundlich isotherm showed the lowest overall error for all error functions and a significantly high R^2 value (~0.996). Therefore, the Freundlich model is considered the best isotherm model for describing the adsorption of phosphate contaminants in wastewater by MIL-53(Al).

Table 4. Results of the error function analysis of the isotherm models at RT.

Isotherm	Parameters		ERRSQ	ARE	HYBRID
Langmuir	Qm k_L	238.10 (mg/g) 0.21 (L/g)	5822.93	32.74	3639.81
Freundlich	k_F n	105.18 6.69 (L/g)	90.64	2.69	2.69
Temkin	AT BT	394 (mg/g) 19.45	875.10	10.69	10.96

Through the completion of error functions, the adsorption system within MIL-53(Al) and Na_2HPO_4 might be suitable for the Elovich and Freundlich kinetic and isotherm models, respectively. This also means that the system's adsorption coexists with chemical adsorption and physical adsorption. In addition to its mesoporous characteristics, MIL-53(Al) showed a positive charge in most pH (1~12) values, which promoted the adsorption and enhanced binding with the strong electronegative [101]. Using a zeta potential meter, we also confirmed that the positive surface potential of MIL-53(Al) varies at different concentrations of Na_2HPO_4. Specifically, the surface potential measured was 25.42 mV in an 80 ppm Na_2HPO_4 solution and 17.42 mV in a 165 ppm Na_2HPO_4 solution. This confirmed physical adsorption. In addition to its mesoporous characteristics, MIL-53(Al) has the potential to adsorb and remove anionic compounds in a wide pH range. It was observed that the pH remained relatively stable within our operating concentration range, staying approximately between pH 7.5 and 8.5 ([Na_2HPO_4] 20~320 ppm). However, when we conducted experiments by adjusting the pH while keeping the concentration of Na_2HPO_4 constant (e.g., 20 ppm), we discovered that the substances used to modify the pH (such as HCl and H_3PO_4 for acids and NaOH for bases) significantly impacted the experimental measurements. This is likely due to excessive competitive adsorption, which can render the results meaningless. As a result, we conclude in this work that the optimal operating pH for MIL-53(Al) is around 7 to 9. Excessive alkaline ions might lead to severe chemical reactions, potentially damaging the MIL-53(Al) crystal structure. Similar observations have been reported in the literature as well [102]. A recent study also mentioned that in addition to the advantages of porosity, the main adsorptive sites were Al and O in the 2D MIL-53(Al) for removing fluoride [101]. In this study, the hydrolysis of disodium hydrogen phosphate produces phosphate ions, specifically $HPO4^{2-}$ and $PO4^{3-}$. Based on hydrogen bonding and van der Waals forces between aluminum and phosphorus, as well as the influence of positively charged aluminum atoms, we believe that the adsorption sites of MIL-53(Al) for disodium hydrogen phosphate are likely located near the Al and O atoms, consistent with findings in the literature. This explains the detection of AlPO4 in the XRD pattern after the prolonged immersion of MIL-53(Al) powder in an aqueous solution of sodium dihydrogen phosphate. In Table S3, we present the comparative values of adsorption in this study with other studies that revealed an excellent phosphate adsorption performance. We also tried to adjust the sulfate concentration to two times the phosphate concentration of raw water and evaluated the adsorption trend within 180 min, as shown in Figure S2. The results showed that there was no significant adsorption of sulfate, indicating that MIL-53(Al) has a very high selective adsorption of phosphate. This may be due to the fact that anion adsorption follows a selectivity sequence consistent with the Hofmeister series. To achieve selective phosphate adsorption, an anti-Hofmeister-type adsorbent is therefore required [103].

3.5. Adsorption and Desorption of MIL-53(Al) Fiber Module

For a sustainable design, recyclable modules are essential for the recycling and reuse of phosphates. Our design imitates the filter concept; the fiber-like MIL-53(Al) structure was created by mixing the MOF powders with appropriate hybrid polymers. Liquid-induced phase separation (LIPS) is carried out in water by injecting precursors through a multi-layer syringe so that microporous hollow fibers are formed (for details, please refer to the experimental section). The MIL-53 hollow fiber we designed has an overall diameter of 2 mm and a middle hole diameter of 1 mm. The wall is composed of MIL-53(Al) and conductive carbon arranged from the inside to the outside, with a thickness ratio of 3:2 (Figure 8a–d). There are two reasons why the outer periphery is covered with carbon: first, the carbon is hydrophobic, allowing the filtered liquid to flow through the inner hollow part; second, the conductive carbon can provide the transmission current needed for the subsequent hollow fiber heating. Current MOF hollow fiber filtration experiments use a module consisting of hundreds of single hollow fibers tightly attached to a single tube bundle. The length is approximately 10 cm after cutting, and the bundle is placed inside a stainless steel filter tube. A 20 ppm sodium phosphate solution (200 mL) was supplied with circulating speed (170 mL/min) by a peristaltic pump from bottom to top.

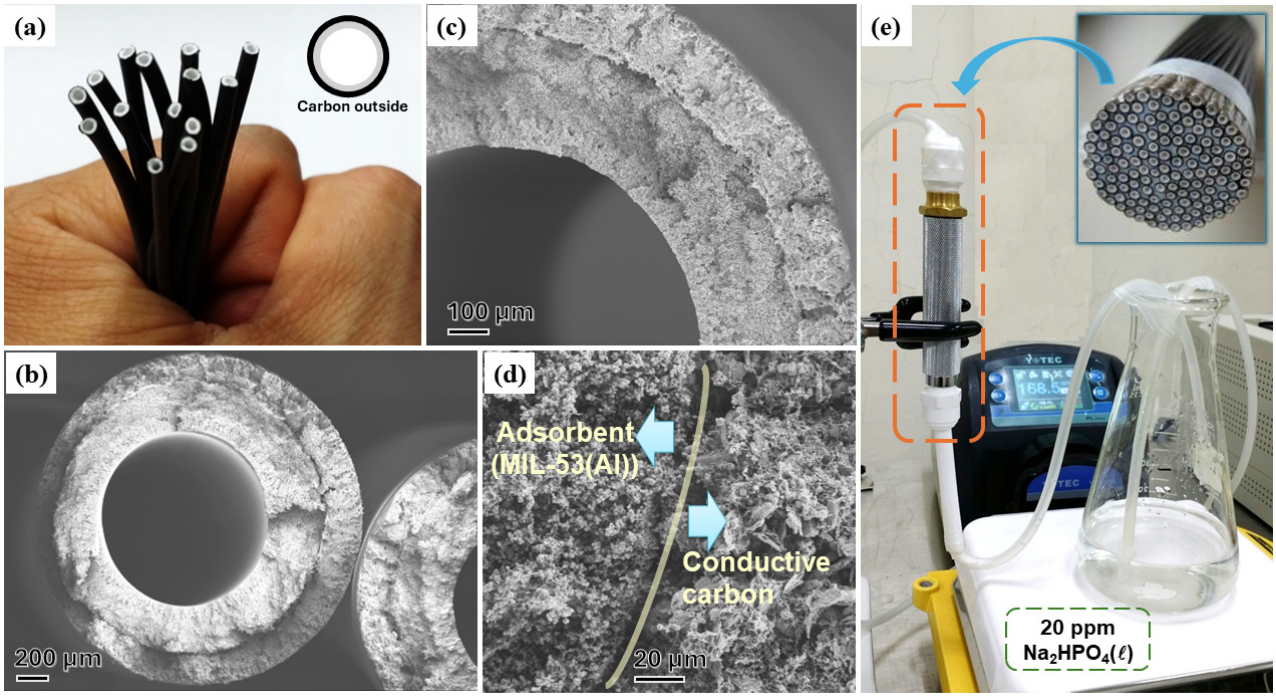


Figure 8. (**a**) Hollow fibers with double layers of MIL-53(Al) and conductive carbon arranged from the inside to the outside. (**b**) Cross-sectional SEM image of hollow fibers. (**c**) Small magnification and (**d**) large magnification showing that the wall of hollow fibers is composed of MIL-53(Al) and conductive carbon from the inside to the outside, with a thickness ratio of 3:2. (**e**) Modular MOF hollow fiber filtration system, including filter element, phosphate solution, glass bottle, peristaltic pump, and stirring plate.

As shown in Figure 9a, we placed one hollow fiber module directly into the Na_2HPO_4 solution with static water and used the peristaltic pump to circulate another Na_2HPO_4 solution for adsorption. Then, we detected the decrease in $PO4^{3-}$ concentration in the solution for comparison. Compared with MIL-53(Al) powder dispersed in the solution, the overall Na_2HPO_4 adsorption rate becomes lower after forming the module. This is due to the total surface area effect. In order to increase the contact probability between the solute and the inner wall of the hollow fiber, we also use a circulation method. From the comparison between the circulation and static methods, we found that the adsorption

rate of the circulation mode (170 mL/min) is five times that of static placement. After four hours of adsorption experiments, the adsorption capacity of the circulation module reached 60.6% of the original total amount of Na_2HPO_4. In contrast, the static solution showed an adsorption capacity of merely 13.8%. In the desorption experiment, for the sake of simplicity, we prepared three modules after four hours of adsorption of the circulating solution and placed them in new stainless steel filter tubes. Each new module was placed in room-temperature deionized water, 75 °C deionized water, and a deionized water solution containing 40 ppm NaCl, respectively. The various desorption experiments were carried out over the same 4 h cycle, and each solution volume was controlled at 200 mL. From the detection of the desorbed phosphorus element in the solution, we realized that increasing the temperature was not positive for desorption, which could be consistent with the Freundlich isotherm model of the system.

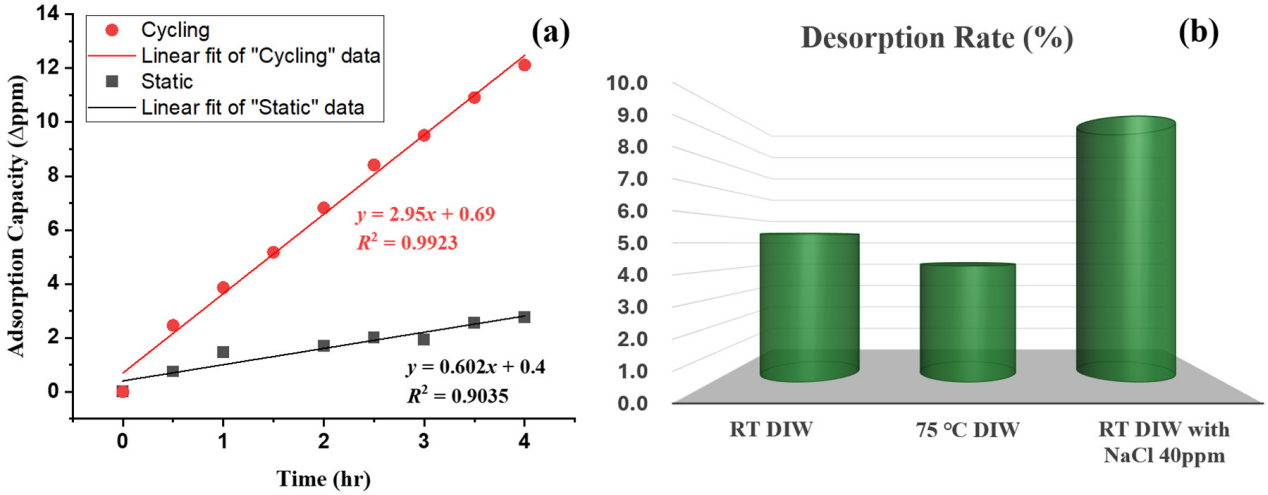


Figure 9. (**a**) Phosphate adsorption rates of static and cycling phosphate solutions after modularization. (**b**) Comparison of phosphate desorption using cold water, hot water, and salt water.

4. Conclusions

The green-synthesized mesoporous MIL-53(Al) MOF nanocrystals were evaluated as an efficient adsorbent for removing phosphates from aqueous solutions. Error functions were used to evaluate kinetic and isotherm models. The Elovich model best fit the kinetic data, indicating a decreasing adsorption rate with increasing capacity. The Freundlich model best described the isotherm data, suggesting a combination of physisorption and chemisorption. Additionally, MIL-53(Al) hollow fiber modules showed promising results for the first time in phosphate adsorption and desorption. Current experiments show that ion exchange is a good method for desorbing phosphate. Although there are still many test conditions, follow-up efforts are needed to optimize this system. This study confirms MIL-53(Al) as a stable adsorbent for removing phosphate. Moreover, future modularization will open the possibility of using this technology for phosphate recovery from wastewater.

Supplementary Materials: The following supporting information can be downloaded at: https://www.mdpi.com/article/10.3390/recycling9050074/s1, Figure S1: SEM images showing the morphology of MIL-53(Al); Table S1: Average crystallite sizes calculated using the Scherrer equation; Table S1: Q_e and experiment results determined using the Langmuir, Freundlich, and Tempkin isotherms; Table S3. A summary of research on phosphate removal using various MOFs; Figure S2. Selective adsorption of coexisting ions of phosphate and sulfate.

Author Contributions: Conceptualization, H.-M.C.; Methodology, S.-F.W. and H.-M.C.; Validation, H.-M.C.; Formal analysis, S.-F.W. and H.-M.C.; Investigation, S.-F.W. and H.-M.C.; Resources, S.-F.W.; Data curation, S.-F.W. and H.-M.C.; Writing—original draft, S.-F.W. and H.-M.C.; Writing—review and editing, H.-M.C.; Visualization, H.-M.C.; Supervision, H.-M.C.; Project administration, H.-M.C.;

Funding acquisition, H.-M.C. All authors have read and agreed to the published version of the manuscript.

Funding: This research was financially supported by the National Science and Technology Council (Grant No. NSTC 113-2740-M-006-002).

Data Availability Statement: The data presented in this study are available on request from the corresponding author.

Acknowledgments: This study was supported by the National Science and Technology Council (grant no. NSTC 113-2740-M-006-002). Shein-Fu Wu and Hsin-Ming Cheng acknowledges the financial of the postdoctoral researcher, Grant No. NSTC 113-2811-M-006-004 and NSTC 113-2811-M-006-017, respectively. The authors also gratefully acknowledge the use of the characteristic equipment belonging to the Core Facility Center of National Cheng Kung University, especially the ICP-MS (ICP000400) and the hollow fiber manufacturing equipment of AuraMat Co., Ltd. and the Industrial Technology Research Institute (ITRI). H. M. Cheng thanks Chin-Chih Tai and Yun-Hsin Wang for their assistance in making hollow fibers, Apinan Sanongsin and Sripansuang Tangsuwanjinda for organizing the diagrams, and Pham Tran My Dung for designing the illustration.

Conflicts of Interest: The authors declare that they have no known competing financial interests or personal relationships that could have appeared to influence the work reported in this paper.

References

1. Kruse, J.; Abraham, M.; Amelung, W.; Baum, C.; Bol, R.; Kühn, O.; Lewandowski, H.; Niederberger, J.; Oelmann, Y.; Rüger, C.; et al. Innovative methods in soil phosphorus research: A review. *J. Plant Nutr. Soil Sci.* **2015**, *178*, 43–88. [CrossRef] [PubMed]
2. Cordell, D.; White, S. Peak Phosphorus: Clarifying the Key Issues of a Vigorous Debate about Long-Term Phosphorus Security. *Sustainability* **2011**, *3*, 2027–2049. [CrossRef]
3. Cordell, D.; White, S. Life's bottleneck: Sustaining the world's Phosphorus for a Food Secure Future. *Annu. Rev. Environ. Resour.* **2014**, *39*, 161–188. [CrossRef]
4. Jacoby, R.; Peukert, M.; Succurro, A.; Koprivova, A.; Kopriva, S. The Role of Soil Microorganisms in Plant Mineral Nutrition-Current Knowledge and Future Directions. *Front. Plant Sci.* **2017**, *8*, 1617. [CrossRef]
5. Westheimer, F.H. Why Nature Chose Phosphates. *Science* **1987**, *235*, 1173–1178. [CrossRef]
6. Al-Fariss, T.F.; Ozbelge, H.O.; El-Shall, H.S. On the Phosphate Rock Beneficiation for the Production of Phosphoric Acid in Saudi Arabia. *J. King Saud Univ.-Eng. Sci.* **1992**, *4*, 13–31. [CrossRef]
7. Miller, D.; Wiener, E.-M.; Turowski, A.; Thunig, C.; Hoffmann, H. O/W emulsions for cosmetics products stabilized by alkyl phosphates—Rheology and storage tests. *Colloids Surf. A Physicochem. Eng. Asp.* **1999**, *152*, 155–160. [CrossRef]
8. Zheng, X.; Yan, X.; Qin, G.; Zhou, R.; Wu, J.; Wei, Z. Soil acidification and phosphorus enrichment enhanced silicon mobility in a Hydragric Anthrosol. *J. Soils Sediments* **2021**, *21*, 3107–3116. [CrossRef]
9. Andersson, K.O.; Tighe, M.K.; Guppy, C.N.; Milham, P.J.; McLaren, T.I. Incremental acidification reveals phosphorus release dynamics in alkaline vertic soils. *Geoderma* **2015**, *259–260*, 35–44. [CrossRef]
10. He, G.; Lao, Q.; Jin, G.; Zhu, Q.; Chen, F. Increasing eutrophication driven by the increase of phosphate discharge in a subtropical bay in the past 30 years. *Front. Mar. Sci.* **2023**, *10*, 1184421. [CrossRef]
11. Hieltjes, A.H.M.; Lijklema, L. Fractionation of Inorganic Phosphates in Calcareous Sediments. *J. Environ. Qual.* **1980**, *9*, 405–407. [CrossRef]
12. House, W.A.; Denison, F.H. Exchange of Inorganic Phosphate between River Waters and Bed-Sediments. *Environ. Sci. Technol.* **2002**, *36*, 4295–4301. [CrossRef]
13. Alsafasfeh, A.; Alagha, L. Recovery of Phosphate Minerals from Plant Tailings Using Direct Froth Flotation. *Minerals* **2017**, *7*, 145. [CrossRef]
14. Mithra, S.S.; Ramesh, S.T.; Gandhimathi, R.; Nidheesh, P.V. Studies on the removal of phosphate from water by electrocoagulation with aluminium plate electrodes. *Environ. Eng. Manag. J.* **2017**, *16*, 2293.
15. Li, J.; Jin, Q.; Liang, Y.; Geng, J.; Xia, J.; Chen, H.; Yun, M. Highly Efficient Removal of Nitrate and Phosphate to Control Eutrophication by the Dielectrophoresis-Assisted Adsorption Method. *Int. J. Environ. Res. Public Health* **2022**, *19*, 1890. [CrossRef]
16. Kumararaja, P.; Suvana, S.; Saraswathy, R.; Lalitha, N.; Muralidhar, M. Mitigation of eutrophication through phosphate removal by aluminium pillared bentonite from aquaculture discharge water. *Ocean Coast. Manag.* **2019**, *182*, 104951. [CrossRef]
17. Mehrabi, N.; Soleimani, M.; Sharififard, H.; Madadi Yeganeh, M. Optimization of phosphate removal from drinking water with activated carbon using response surface methodology (RSM). *Desalination Water Treat.* **2016**, *57*, 15613–15618. [CrossRef]
18. Boeykens, S.P.; Piol, M.N.; Samudio Legal, L.; Saralegui, A.B.; Vázquez, C. Eutrophication decrease: Phosphate adsorption processes in presence of nitrates. *J. Environ. Manag.* **2017**, *203*, 888–895. [CrossRef]
19. Alagha, O.; Manzar, M.S.; Zubair, M.; Anil, I.; Mu'azu, N.D.; Qureshi, A. Comparative Adsorptive Removal of Phosphate and Nitrate from Wastewater Using Biochar-MgAl LDH Nanocomposites: Coexisting Anions Effect and Mechanistic Studies. *Nanomaterials* **2020**, *10*, 336. [CrossRef]

20. Maia, M.A.; Dotto, G.L.; Perez-Lopez, O.W.; Gutterres, M. Phosphate removal from industrial wastewaters using layered double hydroxides. *Environ. Technol.* **2021**, *42*, 3095–3105. [CrossRef]
21. Park, J.Y.; Lee, J.; Go, G.-M.; Jang, B.; Cho, H.-B.; Choa, Y.-H. Removal performance and mechanism of anti-eutrophication anions of phosphate by CaFe layered double hydroxides. *Appl. Surf. Sci.* **2021**, *548*, 149157. [CrossRef]
22. Yadav, D.; Kumar, P.; Kapur, M.; Mondal, M.K. Phosphate removal from aqueous solutions by nano-alumina for the effective remediation of eutrophication. *Environ. Prog. Sustain. Energy* **2019**, *38*, S77–S85. [CrossRef]
23. Awual, M.R. Efficient phosphate removal from water for controlling eutrophication using novel composite adsorbent. *J. Clean. Prod.* **2019**, *228*, 1311–1319. [CrossRef]
24. Ashfaq, M.H.; Shahid, S.; Javed, M.; Iqbal, S.; Hakami, O.; Aljazzar, S.O.; Fatima, U.; Elkaeed, E.B.; Pashameah, R.A.; Alzahrani, E.; et al. Controlled growth of TiO_2/Zeolite nanocomposites for simultaneous removal of ammonium and phosphate ions to prevent eutrophication. *Front. Mater.* **2022**, *9*, 1007485. [CrossRef]
25. Abrahams, B.F.; Hoskins, B.F.; Michail, D.M.; Robson, R. Assembly of porphyrin building blocks into network structures with large channels. *Nature* **1994**, *369*, 727–729. [CrossRef]
26. Kitagawa, S.; Kitaura, R.; Noro, S.-I. Functional Porous Coordination Polymers. *Angew. Chem. Int. Ed.* **2004**, *43*, 2334–2375. [CrossRef]
27. Ferey, G. ChemInform Abstract: Hybrid Porous Solids: Past, Present, Future. *Chem. Soc. Rev.* **2008**, *39*, 191–214. [CrossRef] [PubMed]
28. Horike, S.; Shimomura, S.; Kitagawa, S. Soft porous crystals. *Nat. Chem.* **2009**, *1*, 695–704. [CrossRef]
29. Farha, O.K.; Hupp, J.T. Rational Design, Synthesis, Purification, and Activation of Metal−Organic Framework Materials. *Acc. Chem. Res.* **2010**, *43*, 1166–1175. [CrossRef]
30. Zhou, H.-C.L.; Jeffrey, R.; Yaghi Omar, M. Introduction to Metal–Organic Frameworks. *Chem. Rev.* **2012**, *112*, 673–674. [CrossRef]
31. Furukawa, H.; Cordova, K.E.; O'Keeffe, M.; Yaghi, O.M. The Chemistry and Applications of Metal-Organic Frameworks. *Science* **2013**, *341*, 1230444. [CrossRef] [PubMed]
32. Foo, M.L.; Matsuda, R.; Kitagawa, S. Functional Hybrid Porous Coordination Polymers. *Chem. Mater.* **2014**, *26*, 310–322. [CrossRef]
33. Eddaoudi, M.; Sava, D.F.; Eubank, J.F.; Adil, K.; Guillerm, V. Zeolite-like metal–organic frameworks (ZMOFs): Design, synthesis, and properties. *Chem. Soc. Rev.* **2015**, *44*, 228–249. [CrossRef]
34. Li, J.-R.; Kuppler, R.J.; Zhou, H.-C. Selective gas adsorption and separation in metal–organic frameworks. *Chem. Soc. Rev.* **2009**, *38*, 1477–1504. [CrossRef]
35. Peng, Y.; Krungleviciute, V.; Eryazici, I.; Hupp, J.T.; Farha, O.K.; Yildirim, T. Methane Storage in Metal–Organic Frameworks: Current Records, Surprise Findings, and Challenges. *J. Am. Chem. Soc.* **2013**, *135*, 11887–11894. [CrossRef]
36. Mason, J.A.; Veenstra, M.; Long, J.R. Evaluating metal–organic frameworks for natural gas storage. *Chem. Sci.* **2014**, *5*, 32–51. [CrossRef]
37. Liang, L.; Liu, C.; Jiang, F.; Chen, Q.; Zhang, L.; Xue, H.; Jiang, H.-L.; Qian, J.; Yuan, D.; Hong, M. Carbon dioxide capture and conversion by an acid-base resistant metal-organic framework. *Nat. Commun.* **2017**, *8*, 1233. [CrossRef]
38. Li, J.-R.; Sculley, J.; Zhou, H.-C. Metal–Organic Frameworks for Separations. *Chem. Rev.* **2012**, *112*, 869–932. [CrossRef]
39. Horcajada, P.; Serre, C.; Vallet-Regí, M.; Sebban, M.; Taulelle, F.; Férey, G. Metal–Organic Frameworks as Efficient Materials for Drug Delivery. *Angew. Chem. Int. Ed.* **2006**, *45*, 5974–5978. [CrossRef]
40. Lee, J.; Farha, O.K.; Roberts, J.; Scheidt, K.A.; Nguyen, S.T.; Hupp, J.T. Metal–organic framework materials as catalysts. *Chem. Soc. Rev.* **2009**, *38*, 1450–1459. [CrossRef]
41. Ke, F.; Qiu, L.-G.; Yuan, Y.-P.; Peng, F.-M.; Jiang, X.; Xie, A.-J.; Shen, Y.-H.; Zhu, J.-F. Thiol-functionalization of metal-organic framework by a facile coordination-based postsynthetic strategy and enhanced removal of Hg^{2+} from water. *J. Hazard. Mater.* **2011**, *196*, 36–43. [CrossRef]
42. Khan, N.A.; Hasan, Z.; Jhung, S.H. Adsorptive removal of hazardous materials using metal-organic frameworks (MOFs): A review. *J. Hazard. Mater.* **2013**, *244–245*, 444–456. [CrossRef]
43. Saleem, H.; Rafique, U.; Davies, R.P. Investigations on post-synthetically modified UiO-66-NH_2 for the adsorptive removal of heavy metal ions from aqueous solution. *Microporous Mesoporous Mater.* **2016**, *221*, 238–244. [CrossRef]
44. Kumar, P.; Pournara, A.; Kim, K.-H.; Bansal, V.; Rapti, S.; Manos, M.J. Metal-organic frameworks: Challenges and opportunities for ion-exchange/sorption applications. *Prog. Mater. Sci.* **2017**, *86*, 25–74. [CrossRef]
45. Peng, Y.; Huang, H.; Zhang, Y.; Kang, C.; Chen, S.; Song, L.; Liu, D.; Zhong, C. A versatile MOF-based trap for heavy metal ion capture and dispersion. *Nat. Commun.* **2018**, *9*, 187. [CrossRef]
46. Feng, M.; Zhang, P.; Zhou, H.-C.; Sharma, V.K. Water-stable metal-organic frameworks for aqueous removal of heavy metals and radionuclides: A review. *Chemosphere* **2018**, *209*, 783–800. [CrossRef]
47. Lu, M.; Deng, Y.; Luo, Y.; Lv, J.; Li, T.; Xu, J.; Chen, S.-W.; Wang, J. Graphene Aerogel–Metal–Organic Framework-Based Electrochemical Method for Simultaneous Detection of Multiple Heavy-Metal Ions. *Anal. Chem.* **2019**, *91*, 888–895. [CrossRef]
48. Efome, J.E.; Rana, D.; Matsuura, T.; Lan, C.Q. Insight Studies on Metal-Organic Framework Nanofibrous Membrane Adsorption and Activation for Heavy Metal Ions Removal from Aqueous Solution. *ACS Appl. Mater. Interfaces* **2018**, *10*, 18619–18629. [CrossRef]
49. Liang, H.; Yao, A.; Jiao, X.; Li, C.; Chen, D. Fast and Sustained Degradation of Chemical Warfare Agent Simulants Using Flexible Self-Supported Metal–Organic Framework Filters. *ACS Appl. Mater. Interfaces* **2018**, *10*, 20396–20403. [CrossRef]

50. Jamshidifard, S.; Koushkbaghi, S.; Hosseini, S.; Rezaei, S.; Karamipour, A.; Jafari rad, A.; Irani, M. Incorporation of UiO-66-NH_2 MOF into the PAN/chitosan nanofibers for adsorption and membrane filtration of Pb(II), Cd(II) and Cr(VI) ions from aqueous solutions. *J. Hazard. Mater.* **2019**, *368*, 10–20. [CrossRef]
51. Kalaj, M.; Bentz, K.C.; Ayala, S., Jr.; Palomba, J.M.; Barcus, K.S.; Katayama, Y.; Cohen, S.M. MOF-Polymer Hybrid Materials: From Simple Composites to Tailored Architectures. *Chem. Rev.* **2020**, *120*, 8267–8302. [CrossRef]
52. Xu, G.-R.; An, Z.-H.; Xu, K.; Liu, Q.; Das, R.; Zhao, H.-L. Metal organic framework (MOF)-based micro/nanoscaled materials for heavy metal ions removal: The cutting-edge study on designs, synthesis, and applications. *Coord. Chem. Rev.* **2021**, *427*, 213554. [CrossRef]
53. Lin, K.-Y.A.; Chen, S.-Y.; Jochems, A.P. Zirconium-based metal organic frameworks: Highly selective adsorbents for removal of phosphate from water and urine. *Mater. Chem. Phys.* **2015**, *160*, 168–176. [CrossRef]
54. Xie, Q.; Li, Y.; Lv, Z.; Zhou, H.; Yang, X.; Chen, J.; Guo, H. Effective Adsorption and Removal of Phosphate from Aqueous Solutions and Eutrophic Water by Fe-based MOFs of MIL-101. *Sci. Rep.* **2017**, *7*, 3316. [CrossRef]
55. Liu, R.; Chi, L.; Wang, X.; Wang, Y.; Sui, Y.; Xie, T.; Arandiyan, H. Effective and selective adsorption of phosphate from aqueous solution via trivalent-metals-based amino-MIL-101 MOFs. *Chem. Eng. J.* **2019**, *357*, 159–168. [CrossRef]
56. Warfsmann, J.; Tokay, B.; Champness, N.R. Synthesis of hydrophobic MIL-53(Al) nanoparticles in low molecular weight alcohols: Systematic investigation of solvent effects. *CrystEngComm* **2018**, *20*, 4666–4675. [CrossRef]
57. Hou, J.; Ashling, C.W.; Collins, S.M.; Krajnc, A.; Zhou, C.; Longley, L.; Johnstone, D.N.; Chater, P.A.; Li, S.; Coulet, M.-V.; et al. Metal-organic framework crystal-glass composites. *Nat. Commun.* **2019**, *10*, 2580. [CrossRef]
58. Loiseau, T.; Serre, C.; Huguenard, C.; Fink, G.; Taulelle, F.; Henry, M.; Bataille, T.; Férey, G. A Rationale for the Large Breathing of the Porous Aluminum Terephthalate (MIL-53) Upon Hydration. *Chem.–A Eur. J.* **2004**, *10*, 1373–1382. [CrossRef]
59. Patil, D.V.; Rallapalli, P.B.S.; Dangi, G.P.; Tayade, R.J.; Somani, R.S.; Bajaj, H.C. MIL-53(Al): An Efficient Adsorbent for the Removal of Nitrobenzene from Aqueous Solutions. *Ind. Eng. Chem. Res.* **2011**, *50*, 10516–10524. [CrossRef]
60. Mounfield, W.P.; Walton, K.S. Effect of synthesis solvent on the breathing behavior of MIL-53(Al). *J. Colloid Interface Sci.* **2015**, *447*, 33–39. [CrossRef]
61. Nishida, J.; Fayer, M.D. Guest Hydrogen Bond Dynamics and Interactions in the Metal–Organic Framework MIL-53(Al) Measured with Ultrafast Infrared Spectroscopy. *J. Phys. Chem. C* **2017**, *121*, 11880–11890. [CrossRef]
62. Mota, J.P.B.; Martins, D.; Lopes, D.; Catarino, I.; Bonfait, G. Structural Transitions in the MIL-53(Al) Metal–Organic Framework upon Cryogenic Hydrogen Adsorption. *J. Phys. Chem. C* **2017**, *121*, 24252–24263. [CrossRef]
63. Priyanthi Perera, S.; Tai, C.-C. Hollow Fibres. US8669200B2, 11 March 2014.
64. Tai, C.-C. A Hollow Fiber for Adsorption or Filtration and a Method for Manufacturing the Same. I504790, 21 October 2015.
65. Yot, P.G.; Boudene, Z.; Macia, J.; Granier, D.; Vanduyfhuys, L.; Verstraelen, T.; Van Speybroeck, V.; Devic, T.; Serre, C.; Férey, G.; et al. Metal–organic frameworks as potential shock absorbers: The case of the highly flexible MIL-53(Al). *Chem. Commun.* **2014**, *50*, 9462–9464. [CrossRef]
66. Wong-Ng, W.; Nguyen, H.G.; Espinal, L.; Siderius, D.W.; Kaduk, J.A. Powder X-ray structural studies and reference diffraction patterns for three forms of porous aluminum terephthalate, MIL-53(A1). *Powder Diffr.* **2019**, *34*, 216–226. [CrossRef]
67. Muniz, F.T.L.; Miranda, M.A.R.; Morilla dos Santos, C.; Sasaki, J.M. The Scherrer equation and the dynamical theory of X-ray diffraction. *Acta Crystallogr. Sect. A* **2016**, *72*, 385–390. [CrossRef]
68. Zhou, M.; Wu, Y.-n.; Qiao, J.; Zhang, J.; McDonald, A.; Li, G.; Li, F. The removal of bisphenol A from aqueous solutions by MIL-53(Al) and mesostructured MIL-53(Al). *J. Colloid Interface Sci.* **2013**, *405*, 157–163. [CrossRef]
69. Liu, J.-F.; Mu, J.-C.; Qin, R.-X.; Ji, S.-F. Pd nanoparticles immobilized on MIL-53(Al) as highly effective bifunctional catalysts for oxidation of liquid methanol to methyl formate. *Pet. Sci.* **2019**, *16*, 901–911. [CrossRef]
70. Li, C.; Xiong, Z.; Zhang, J.; Wu, C. The Strengthening Role of the Amino Group in Metal–Organic Framework MIL-53(Al) for Methylene Blue and Malachite Green Dye Adsorption. *J. Chem. Eng. Data* **2015**, *60*, 3414–3422. [CrossRef]
71. Salazar, J.M.; Weber, G.; Simon, J.M.; Bezverkhyy, I.; Bellat, J.P. Characterization of adsorbed water in MIL-53(Al) by FTIR spectroscopy and ab-initio calculations. *J. Chem. Phys.* **2015**, *142*, 124702. [CrossRef]
72. Rahmani, E.; Rahmani, M. Al-Based MIL-53 Metal Organic Framework (MOF) as the New Catalyst for Friedel–Crafts Alkylation of Benzene. *Ind. Eng. Chem. Res.* **2018**, *57*, 169–178. [CrossRef]
73. Perea-Cachero, A.; Sánchez-Laínez, J.; Zornoza, B.; Romero-Pascual, E.; Téllez, C.; Coronas, J. Nanosheets of MIL-53(Al) applied in membranes with improved CO_2/N_2 and CO_2/CH_4 selectivities. *Dalton Trans.* **2019**, *48*, 3392–3403. [CrossRef]
74. Wei, Y.; Xia, Y. Pyridine-grafted Cr-based metal–organic frameworks for adsorption and removal of microcystin-LR from aqueous solution. *Environ. Sci. Water Res. Technol.* **2019**, *5*, 577–584. [CrossRef]
75. Sims, R.A.; Harmer, S.L.; Quinton, J.S. The Role of Physisorption and Chemisorption in the Oscillatory Adsorption of Organosilanes on Aluminium Oxide. *Polymers* **2019**, *11*, 410. [CrossRef] [PubMed]
76. Ho, Y.S.; McKay, G. Pseudo-second order model for sorption processes. *Process Biochem.* **1999**, *34*, 451–465. [CrossRef]
77. Moussout, H.; Ahlafi, H.; Aazza, M.; Maghat, H. Critical of linear and nonlinear equations of pseudo-first order and pseudo-second order kinetic models. *Karbala Int. J. Mod. Sci.* **2018**, *4*, 244–254. [CrossRef]
78. Chien, S.H.; Clayton, W.R. Application of Elovich Equation to the Kinetics of Phosphate Release and Sorption in Soils. *Soil Sci. Soc. Am. J.* **1980**, *44*, 265–268. [CrossRef]

79. Wu, F.-C.; Tseng, R.-L.; Juang, R.-S. Characteristics of Elovich equation used for the analysis of adsorption kinetics in dye-chitosan systems. *Chem. Eng. J.* **2009**, *150*, 366–373. [CrossRef]
80. Haque, E.; Jun, J.W.; Jhung, S.H. Adsorptive removal of methyl orange and methylene blue from aqueous solution with a metal-organic framework material, iron terephthalate (MOF-235). *J. Hazard. Mater.* **2011**, *185*, 507–511. [CrossRef] [PubMed]
81. Ho, Y.S.; McKay, G. The kinetics of sorption of divalent metal ions onto sphagnum moss peat. *Water Res.* **2000**, *34*, 735–742. [CrossRef]
82. George William, K.; Serkan, E.; Atakan, Ö.; Özcan, H.K.; Serdar, A. Modelling of Adsorption Kinetic Processes—Errors, Theory and Application. In *Advanced Sorption Process Applications*; Serpil, E., Ed.; IntechOpen: Rijeka, Croatia, 2018; Chapter 10. [CrossRef]
83. Pooresmaeil, M.; Namazi, H. Chapter 14—Application of polysaccharide-based hydrogels for water treatments. In *Hydrogels Based on Natural Polymers*; Chen, Y., Ed.; Elsevier: Amsterdam, The Netherlands, 2020; pp. 411–455. [CrossRef]
84. Ouakouak, A.K.; Youcef, L. Phosphates Removal by Activated Carbon. *Sens. Lett.* **2016**, *14*, 600–605. [CrossRef]
85. Allen, S.J.; McKay, G.; Porter, J.F. Adsorption isotherm models for basic dye adsorption by peat in single and binary component systems. *J. Colloid Interface Sci.* **2004**, *280*, 322–333. [CrossRef] [PubMed]
86. Liu, Y. Some consideration on the Langmuir isotherm equation. *Colloids Surf. A Physicochem. Eng. Asp.* **2006**, *274*, 34–36. [CrossRef]
87. McKay, G.; Otterburn, M.S.; Sweeney, A.G. Kinetics of Colour Removal from Effluent Using Activated Carbon. *J. Soc. Dye. Colour.* **1980**, *96*, 576–579. [CrossRef]
88. Moon, H.; Kook Lee, W. Intraparticle diffusion in liquid-phase adsorption of phenols with activated carbon in finite batch adsorber. *J. Colloid Interface Sci.* **1983**, *96*, 162–171. [CrossRef]
89. Al Duri, B.; McKay, G. Basic dye adsorption on carbon using a solid-phase diffusion model. *Chem. Eng. J.* **1988**, *38*, 23–31. [CrossRef]
90. Saadi, R.; Saadi, Z.; Fazaeli, R.; Fard, N.E. Monolayer and multilayer adsorption isotherm models for sorption from aqueous media. *Korean J. Chem. Eng.* **2015**, *32*, 787–799. [CrossRef]
91. Haghseresht, F.; Lu, G.Q. Adsorption Characteristics of Phenolic Compounds onto Coal-Reject-Derived Adsorbents. *Energy Fuels* **1998**, *12*, 1100–1107. [CrossRef]
92. Reed, B.E.; Matsumoto, M.R. Modeling Cadmium Adsorption by Activated Carbon Using the Langmuir and Freundlich Isotherm Expressions. *Sep. Sci. Technol.* **1993**, *28*, 2179–2195. [CrossRef]
93. Özer, A.; Pirinççi, H.B. The adsorption of Cd(II) ions on sulphuric acid-treated wheat bran. *J. Hazard. Mater.* **2006**, *137*, 849–855. [CrossRef]
94. Desta, M.B. Batch Sorption Experiments: Langmuir and Freundlich Isotherm Studies for the Adsorption of Textile Metal Ions onto Teff Straw (*Eragrostis tef*) Agricultural Waste. *J. Thermodyn.* **2013**, *2013*, 375830. [CrossRef]
95. Balarak, D.; Mostafapour, F.; Azarpira, H.; Joghataei, A. Langmuir, Freundlich, Temkin and Dubinin–Radushkevich Isotherms Studies of Equilibrium Sorption of Zn^{2+} Unto Phosphoric Acid Modified Rice Husk. *IOSR J. Appl. Chem.* **2012**, *3*, 38–45.
96. Hamdaoui, O.; Naffrechoux, E. Modeling of adsorption isotherms of phenol and chlorophenols onto granular activated carbon: Part I. Two-parameter models and equations allowing determination of thermodynamic parameters. *J. Hazard. Mater.* **2007**, *147*, 381–394. [CrossRef]
97. Subramanyam, B.; Das, A. Linearised and non-linearised isotherm models optimization analysis by error functions and statistical means. *J. Environ. Health Sci. Eng.* **2014**, *12*, 92. [CrossRef] [PubMed]
98. Demirbas, E.; Kobya, M.; Konukman, A.E.S. Error analysis of equilibrium studies for the almond shell activated carbon adsorption of Cr(VI) from aqueous solutions. *J. Hazard. Mater.* **2008**, *154*, 787–794. [CrossRef]
99. Namasivayam, C.; Yamuna, R.T. Adsorption of chromium (VI) by a low-cost adsorbent: Biogas residual slurry. *Chemosphere* **1995**, *30*, 561–578. [CrossRef]
100. Foo, K.Y.; Hameed, B.H. Insights into the modeling of adsorption isotherm systems. *Chem. Eng. J.* **2010**, *156*, 2–10. [CrossRef]
101. Huang, L.; Yang, Z.; Alhassan, S.I.; Luo, Z.; Song, B.; Jin, L.; Zhao, Y.; Wang, H. Highly efficient fluoride removal from water using 2D metal-organic frameworks MIL-53(Al) with rich Al and O adsorptive centers. *Environ. Sci. Ecotechnol.* **2021**, *8*, 100123. [CrossRef]
102. Qian, X.; Yadian, B.; Wu, R.; Long, Y.; Zhou, K.; Zhu, B.; Huang, Y. Structure stability of metal-organic framework MIL-53(Al) in aqueous solutions. *Int. J. Hydrogen Energy* **2013**, *38*, 16710–16715. [CrossRef]
103. Awual, M.R.; Jyo, A. Rapid column-mode removal of arsenate from water by crosslinked poly(allylamine) resin. *Water Res.* **2009**, *43*, 1229–1236. [CrossRef]

Disclaimer/Publisher's Note: The statements, opinions and data contained in all publications are solely those of the individual author(s) and contributor(s) and not of MDPI and/or the editor(s). MDPI and/or the editor(s) disclaim responsibility for any injury to people or property resulting from any ideas, methods, instructions or products referred to in the content.